Use of numerical simulation for the identification of underground voids using the MASW test

Hassan Ali[1], Ali Nasseri-Moghaddam[2], Giovanni Cascante[1]
[1]*Department of Civil Engineering - University of Waterloo, ON, Canada*
[2]Inspec-Sol Inc., Waterloo, ON, Canada

2011 Pan-Am CGS Geotechnical Conference

ABSTRACT
The identification of underground voids is very important for any geotechnical site investigation. Geophysical methods are commonly used to locate underground voids; but there are still many limitations to be addressed. This paper presents the results from numerical simulations of MASW tests on laterally non-homogenous media. Surface responses are recorded on a linear seismic array of 101 receivers. Rectangular voids of variable width, height and embedment depth are used. The simulated responses are processed using a commercial package to compute the dispersion curves and frequency-wave number plots. These dispersion curves are used to study the changes induced by the presence of void; from where common patterns are identified. These general patterns can be used to define guidelines for the selection of the optimal MASW test configuration for the detection of voids for a given site condition. The results from these analyses are summarized in a table that shows the effect of the void on the dispersion curve as a function of the void size normalized by the corresponding wavelength.

RÉSUMÉ
L'identification des vides souterrains est très important pour toute enquête géotechnique du site. Les méthodes géophysiques sont couramment utilisés pour localiser des vides souterrains, mais il ya encore beaucoup de limitations à traiter. Cet article présente les résultats des simulations numériques des tests sur des supports MASW latéralement non-homogène. Surface réponses sont enregistrées sur un réseau linéaire de 101 récepteurs sismiques. Vides rectangulaire de largeur variable, hauteur et profondeur d'ancrage sont utilisés. Les réponses simulées sont traitées à l'aide d'un progiciel commercial pour calculer les courbes de dispersion des parcelles et le numéro de la fréquence des ondes. Ces courbes de dispersion sont utilisées pour étudier les changements induits par la présence de vide; d'où des modèles communs sont identifiés. Ces tendances générales peuvent être utilisées pour définir des lignes directrices pour la sélection de la configuration optimale MASW test pour la détection des vides pour un problème de site donné. Les résultats de ces analyses sont résumés dans un tableau qui montre l'effet du vide sur la courbe de dispersion en fonction de la taille des vides normalisée par la longueur d'onde correspondant.

1 INTRODUCTION

Failure of ground surface and subsidence due to underground cavities are major problems around the world. These can cause damage to buildings, foundations, and infrastructure. Due to the non-availability of maps indicating the location of underground excavations, abandoned mines are of particular concern. Turney (1985) reported potential hazard for approximately 13,000 people and 5,000 houses along the Front Range Urban Corridor, Colorado that can be caused by subsidence over abandoned coal mines. Thus, the identification and location of underground cavities in karst prone regions and areas with subsurface excavation is very important.

In spite of improvement in the geophysical methods, identification of sub-surface ground anomalies is still a challenging problem. Ground-penetrating radar has been successfully implemented for shallow depths; yet, problem arises when underground surface consists of high conductivity materials such as clays (Kong et al., 1994). Seismic reflection can be used to locate underground cavities in the presence of horizontal soil layers above and below the void.

Multi-channel analysis of surface waves (MASW) is a geophysical technique that has gained attention and acceptance for the detection of underground voids as reported by Nasseri-Moghaddam et. al., (2007). The MASW technique uses Rayleigh waves for estimating the soil stiffness profile at site. Due to the scattering of Rayleigh waves by the heterogeneities, analytical description is difficult and therefore field experiments and numerical models are carried out to study this problem. Phillips et al. (2004) conducted field tests, experiments on prototypes, and numerical studies and reported areas of high-energy concentrations on the surface response over different voids. Similarly, various numerical models with lateral inhomogeneities showed that the presence of an anomaly causes rippled signals in time. These ripples are more noticeable in the area between the source and void, because part of the incident wave energy is reflected back from the void. It was further mentioned that the width of the void affects the pattern of ripples while embedment depth of void affects the amplitude of reflections. In general, these studies show a good agreement between numerical simulation and experimental results.

In order to study the effect of void size and location different studies are carried out to associate the surface response of a medium to the location and size of void. Philips et al. (2001) performed field and laboratory experiment tests and presented the results in the frequency domain. They reported regions of high energy concentrations in the vicinity of the void and hence suggested the use of power spectral density functions (PSD method) for detection of voids. Shokouhi and Gucunski (2003) used wavelet analysis of the responses

to correlate the width of the high-energy region to the size of the void. Methods discussed above do not consider the embedment depth of the void and are based on the changes of the surface responses. Recently Nasseri-Moghaddam et al. (2007) developed techniques that are useful in locating the void and estimating its embedment depth. However, the application of the MASW method for void detection is usually limited to shallow depths, mostly due to difficulties of generating long wavelengths with high signal-to-noise ratios, and partly because of the lack of understanding of the interaction of embedded voids and Rayleigh waves. In general, these studies show a good agreement between numerical simulation and experimental results.

In this paper, we study the effect of underground void on dispersion curves obtained from numerical models simulating MASW test in the presence of lateral homogeneities. The objective of this research is to provide define strategies for the selection of optimal MASW test configuration for the detection of voids for a given site condition. Numerical data from two dimensional (2D) axis-symmetric models for this study are acquired from Moghaddam (2006). The model comprises of voids having variable width and embedment depth. To understand the influence of array length on underground void; the total surface recording points of the numerical model are divided into three sections, i.e., section1, section2, and section3. Surface responses from these sections are analysed in the time and frequency domain. The 2D-FFT or Frquency-wavnumber (f-k) plots for each model are developed using computer software package SWAN. The f-k plots not only indicate the velocity of the wave propagating but also indicates the energy density within a given time interval. Dispersion curves are calculated using 2D-FFT data from SWAN. These dispersion curves are further evaluated to identify general pattern, which are summarized in a table that shows the effect of void on the dispersion curve as a function of the void size normalized by wavelength.

2 REVIEW OF MASW THEORY

The multi-channel analysis of surface wave (MASW) is a non-destructive technique used for the detection of underground voids. MASW is an extension of SASW method based on the work by Nazarian et al. (1984). It utilizes several transducers for computation of underground responses. The approach of using several transducers effectively allow the removal of noise and help in identification of higher order Rayleigh wave modes (Park et al., 1999). As Rayleigh waves are confined to the near surface of the ground, therefore low energy seismic source is usually recommended for lab and field tests.

Rayleigh waves are dispersive in nature and dispersion of Rayleigh waves are used in the evaluation of sub-surface stiffness profiles. Since the stiffness of soil usually increases with depth, the depth to which Rayleigh wave causes significant displacement increases with increasing wavelength. Low frequency (long wavelength) propagates faster than high frequency (short wavelength). Thus it can be concluded that penetration depth of Rayleigh wave is inversely proportional to its frequency. Usually, maximum penetration depth is considered to be one wavelength in field and laboratory. Frequency spectra and dispersion curve (phase velocity profile) for a site are obtained from the time domain signals. These dispersion curves can be inverted to estimate the shear-modulus profile of the medium (Stoke et al., 1988).

Figure 1 shows configuration of the MASW test. For low energy seismic sources, sledgehammer is commonly used in the industry. Mechanical harmonic sources and passive sources such as ambient noise and micro-tremors have also been used. The source should be able to yield enough energy over the required test frequency range to allow the detection of Rayleigh waves above background noise. Velocity transducers (geophones) are used to collect the surface responses in the low frequency range (4 Hz to 100 Hz); whereas, accelerometers are used for higher frequencies (100 Hz to 5000 Hz) (Cascante et al., 2006). The distance between the source and first receiver determines the largest reliable wavelength in the measurements. On the other hand, the distance between transducers (D) and the sampling rate (δt) determine the smallest reliable wavelength. A common practice is to choose a source to receiver distance equal to at least twice the maximum required wavelength (Hiltunen and Woods, 1989).

3 NUMERICAL MODEL

In order to study the effect of void width and size numerically, finite difference program FLAC (Itasca, 2000) is used. The numerical model simulates wave propagation in a linear elastic continuum that contains a void. Since the induced shear strains are less than 0.001% in MASW test (Gucunski et al., 1996), hence an elastic medium is assumed. In MASW tests, the medium properties and propagation pulse govern wave propagation through the medium. The medium properties include modulus of elasticity E, Poisson ratio ν, mass densityρ, and material damping D. Since material damping is small for low strains and independent of frequency (Santamarina et al., 2001); assumed material damping is ignored.

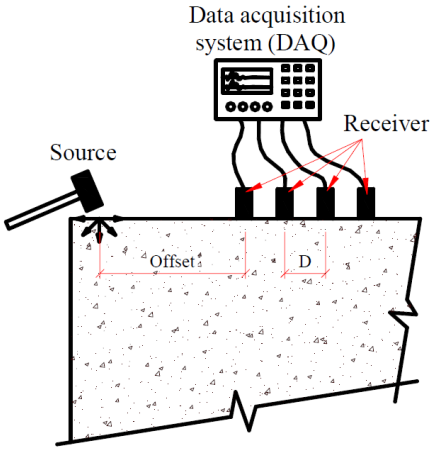

Figure 1: A schematic drawing of MASW test

The selected material properties for the numerical model are Poisson's ratio, $\nu = 0.2$

; density, $\rho = 1600$ (kg/m^3), and modulus of elasticity, E = 19 MPa. Consequently, the corresponding wave velocities are P-wave, V_P = 114.9 m/s, shear wave V_S = 70.3 m/s and Rayleigh wave V_R = 64.08 m/s (Nasseri-Moghaddam, 2006). Figure 2a and 2b illustrate a general sketch of the two-dimensional axisymmetric model used for the simulations. Figure 2a shows the location and embedment depth of void from receiver while Figure 2b represents the array sections considered for this study. Model parameters are adjusted to match theoretical results and to verify that the model accurately predicts the R-wave propagation in a semi-infinite medium. The model consists of a central uniform grid surrounded by a non-uniform grid.

The axis of symmetry is defined at the left end boundary, while quiet boundaries are defined at the right and bottom. To effectively reduce the reflections of R-waves, the boundaries of the numerical model are practically positioned as far from the void as possible. The distance between the receivers and boundary is selected in a manner to ensure that the reflections from the boundary are greater than the main Rayleigh wave arrival at any receivers. Hence, reflections from the boundary can be seen in the time signals of main Rayleigh wave event. Alternatively, reflections from R-wave generated after the interaction of the main R-wave event with the void are practically not affected by boundary reflections because of their geometrical. The maximum running time of the numerical model for all case studies is restricted to t_{max}= 0.23s. The sampling frequency is f = 10^4 Hz (time increment $\delta t = 10^{-4}$s). Lamb source f (t) presented in Equation 1 is applied to all numerical simulations (Lamb, 1904). The forcing function is applied to the left boundary.

$$f(t)=\frac{F_b}{\pi}\frac{\tau}{t^2+\tau^2} \qquad [1]$$

In Equation 1, F_b and τ are constants that modify the amplitude and the frequency content of the force function consequently.

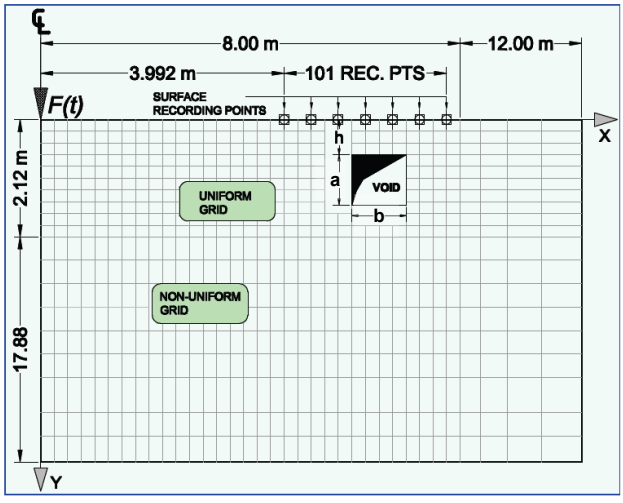

Figure 2a: Configuration of the basic finite difference model showing the location of receiver points and model dimension

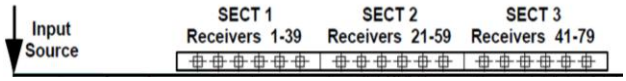

Figure 2b: Configuration of array sections used in the study

4 EXPERIMENTAL METHODOLOGY

Rectangular voids of variable width, height, and embedment depth are introduced in the numerical model. The distance from the source to first (offset distance) and last receivers are 3.992 m and 7.992 m respectively. The width and height of the void ranges from 0.08 to 0.32 m and the embedment depth is changed from 0.08 m to 0.32 m. Surface responses are recorded from a total of 101 recording points as shown in Figure 2a. The maximum and minimum reliable wavelengths considered for the model are λ_{max}= 2.0 m (f = 32 Hz) and λ_{min} = 0.08m (f = 801 Hz) respectively. In order to reduce near-field effects, recording points are located far from the source.

Table 1, presents the width and embedment depth of rectangular voids used in the numerical model. The height of the void remains constant for all models, i.e., a = 0.08m. In Table 1, the models have been named based on the width and embedment depth of the void. For example, b08h08 represents void having width, b= 08 cm and embedment depth h = 08 cm, respectively. To better study the effect of recording points on surface responses; recording points are divided into three sections as illustrated in Figure 2b. Section 1 (1-39) defines array of recording points before void, section 2 (21-59) defines array of recording points centered on void, while section 3 (41-79) defines array of recording points after void, respectively. The length of array in each section is kept constant, i.e., 38 receivers. Further, the calibration of the numerical model is performed by changing model parameters such that the responses measured from numerical model without void matches well with the theoretical model. Details of calibration can be found in (Nasseri-Moghaddam, 2006).

Table 1. Model number and dimensions of voids

Model number	Width (b) [m]	Embedment Depth (h) [m]
b08h08	0.08	0.08
b16h08	0.16	0.08
b32h08	0.32	0.08
b08h16	0.08	0.16
b16h16	0.16	0.16
b32h16	0.32	0.16
b08h32	0.08	0.32
b16h32	0.16	0.32
b32h32	0.32	0.32

5 NUMERICAL RESULTS

5.1 Analysis of results in time domain

Figure 3, shows the typical time traces of surface responses, due to Rayleigh waves, for section 1, 2, and 3. The time window in the Figure is selected in such a way to demonstrate the main features of Rayleigh waves; since the amplitude of other waves is negligible as compared to R-waves. The solid line represents surface response in the presence of void while dash line represents surface response from the no-void case. For completeness purpose the time traces shown in Figure are for void having width 8cm and embedment depth 8cm. In each of the three sections, the arrival of main pulse can be seen. Effect of reflections from void can be clearly observed in section 1 and 2.

5.2 Analysis of results in frequency domain

Figure 4 shows a comparison of the typical Fourier spectra of the vertical displacements obtained from time traces in Figure 3. Similar to previous section, Fourier spectra is shown for no-void (dash line) and void (solid line) case. The dimensions of the void are width 8cm and embedment depth 8cm. The amplitudes of the spectra are normalized based on the section having lowest amplitude. Therefore, for no-void and void cases, the spectra are normalized based on section 3. Fourier spectrum of the no-void case is relatively smooth in all three sections. The minor undulations shown in section 1 can be attributed to the reflection of P-waves from the model boundaries.

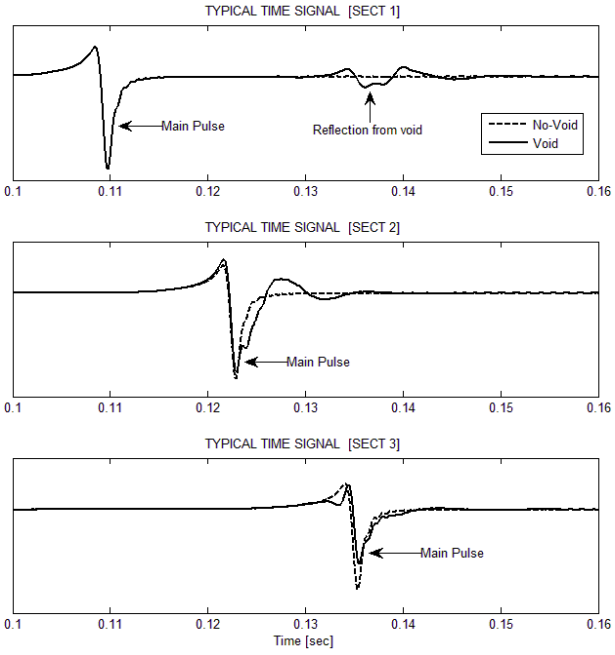

Figure 3: Time responses of section 1, 2, and 3 for b = 0.08m and h = 0.08m. Also shown is the no-void case.

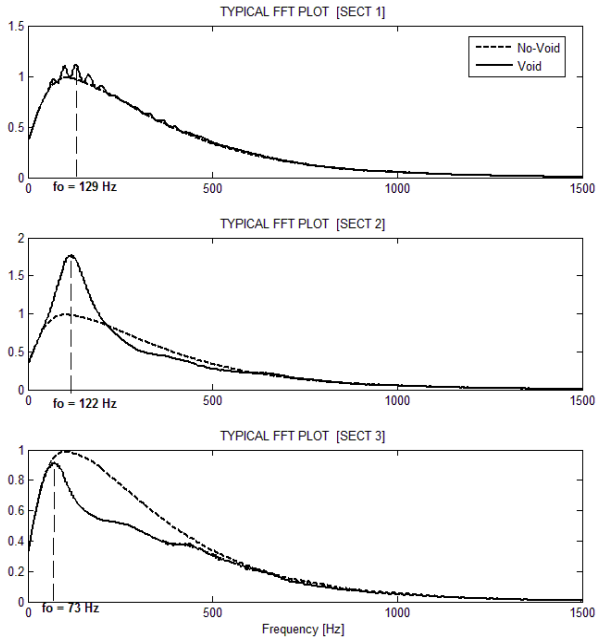

Figure 4: Fourier Transform of section 1, 2, and 3 for b = 0.08m and h = 0.08m. No-void case shown in dashed line.

5.3 Frequency-wavenumber f-k (2D FFT) analysis

In this study a new commercial software package SWAN (Surface Wave ANalysis) is utilized. SWAN is seismic data processing software for data modeling and inversion of surface waves measurements acquired in MASW or REMI model. The surface responses from each model are numerically processed in SWAN to obtain frequency-wavenumber (f-k) plots. Typical f-k plot for no-void and void cases are shown in Figure 5. The contours represent energy amplitude. Observing the spectrum, it can be seen that, the main part of energy (dark blue and cyan color) in this case is between 50 and 100 m/sec. For the evaluation of experimental dispersion curve, these areas of energy concentrations should be searched for local maxima of the spectrum's amplitude. Each white line exiting from the FK spectrum represents velocity. Using f-k plots the direction and apparent velocity of seismic waves can be examined. As we know that $V = f\lambda$ and $\lambda = 1/k$ which leads to the relation $V = f/k$. Thus the slope of a frequency-wavenumber plot is related to the speed of propagation of wave. The wave number range represents the direction of traveling wave, i.e., positive wavenumber shows waves propagating in the forward direction (away from the source), and vice versa. In the Figure, Rayleigh and P – waves can be identified using the slope of f-k plot. The values plotted in Figure 5 are logarithmic values.

5.4 Dispersion curves

A dispersion curve describes the variation in velocity with frequency. Figure 6 shows typical dispersion curves for section 1, 2, and 3 obtained using SWAN for time traces presented in Figure 3. Similar to previous results, comparison have been made between no-void and void case for each section. Solid line in Figure 6 represents

data with the void, while dash line represents data with the no-void model. Dashed horizontal line in each section shows the R-wave velocity. These dispersion curves are obtained by selecting the local maxima from the f-k spectrum. Dispersion curves obtained from the SWAN are smoothed using a Gaussian function having a bandwidth of 10.

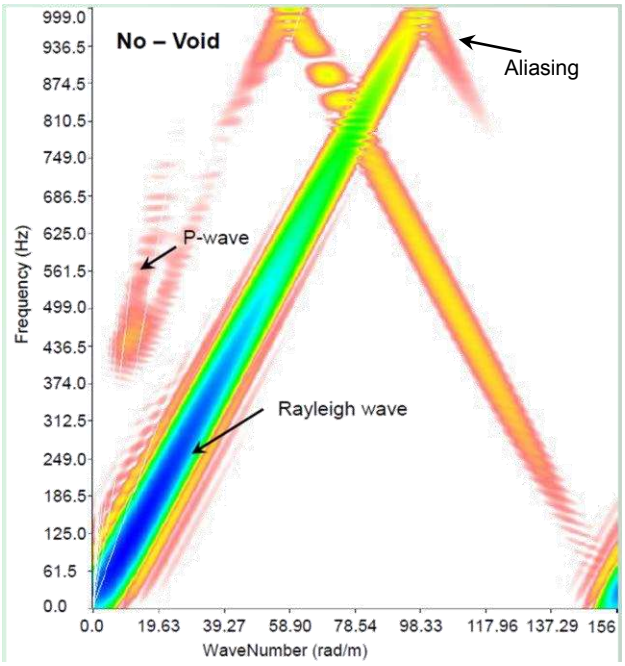

a) 2D FFT plot for no-void case

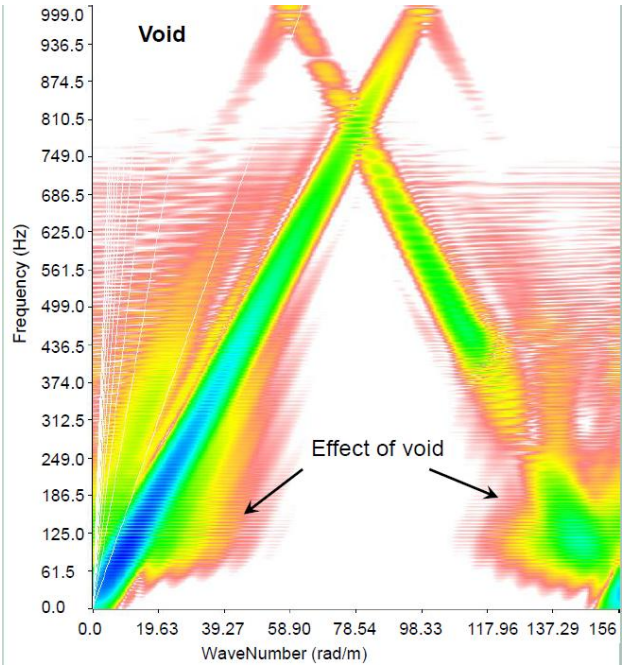

b) 2D plot for case having void (b = 0.08m and h = 0.08m)

Figure 5: Frequency-wave number (2D-FFT) plots

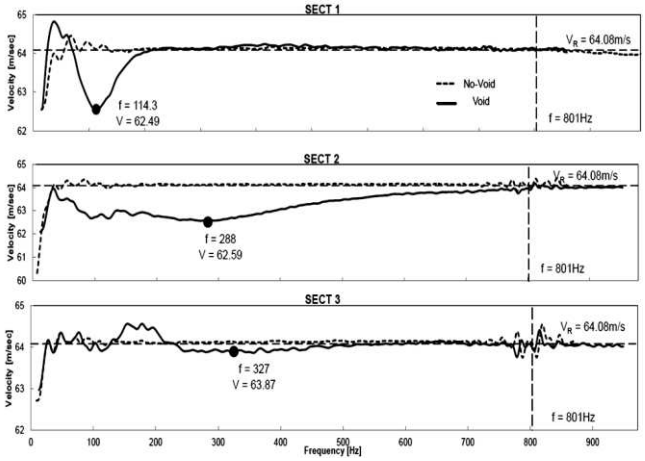

Figure 6: Dispersion Curves of section 1, 2, and 3 for b = 0.08m and h = 0.08m

5.5 Pattern identification and normalized wavelength (λ) tables

Once the dispersion curves were obtained for all models, the next step was to identify the pattern between sections for each model. The pattern identification was based on the trend (change) in frequency for dispersion curves having void and comparing them with the no-void case. This method would ensure that the change in velocity is due the effect of void and not a numerical model error. Figure 6 illustrates this identification of pattern by circular markers on dispersion curves. Velocity and frequency values are also noted for the identified points. These values are then recorded in Table 2. The above procedure is repeated for all models and values are summarized in Table 2.

The table has been divided into three columns which represent the change in the width of void, while rows represent change in sections. Thus going from left to right the width of the void changes from 8cm to 32cm and going from top to bottom represents section 1 to section 3. Within each section, the width of the void remains constant but the embedment depth changes. Hence the nomenclature of the models has been done accordingly. For example S1b08h08 represent section 1 of the void having width 8cm and embedment depth 8cm. To understand the effect of void size on dispersion curve as a function of wavelength; wavelength (λ) is calculated for each section based on the identified pattern. Wavelength is evaluated using the expression

$$\lambda = \frac{V_R}{f} \qquad [2]$$

In the above equation, V_R is the Rayleigh wave velocity (64.08 m/s) and f is frequency obtained from pattern identification. Finally, the normalized wavelength values are obtained using the relation:

$$\lambda_{normalized} = \frac{\lambda}{H} \qquad [3]$$

where H is the sum of void height and embedment depth of void, i.e., (H = a + h). Table 3 shows the percentage difference in velocity between the pattern identified and the Rayleigh wave. The percentage difference is calculated by following expression:

$$\%\Delta V = \frac{V_R - V_1}{V_1} \times 100 \quad [4]$$

In the above expression, V_1 is the pattern identified value. The model nomenclature in Table 3 is similar to Table 2.

For all the numerical models, the surface responses are taken from vertical displacements except for model having width b = 16cm (due to non-availability of vertical displacement values); for which horizontal displacement values are taken. Similarly, due to the large difference between the dispersion curve values for S3b16h08, S3b16h16, and S3b16h32, the pattern identified values are not tabulated in Table 2 and 3.

6. DISCUSSION

From the time traces, it can be observed that the presence of a void has considerable effect on all time traces. Due to the interaction of the incident Rayleigh wave and near boundary of the void, part of the energy is reflected back in the form of R-waves; this can be observed in section 1 marked as reflection from void.

As mentioned in previous section, in homogenous medium the Fourier spectra for no-void model are smooth and its shape does not change with distance, however the amplitude decreases. Maximum energy occurs at a frequency of about 100Hz, which corresponds to a wavelength of 0.6408m ($\lambda = V_R/f$). In the case of void (b = 8cm, h = 8cm), the Fourier spectra are not smooth and different shapes of the spectra indicates that the medium is dispersive. The values at which maximum energy occurs for void case are shown in Figure 4. Higher amplitudes are observed at section over the void and attenuation is observed in section after the void. The results of amplitude variation show that in the presence of void not only energy concentration occurs but also the attenuation happens in certain frequency ranges.

From the results shown in Figure 5, the linearity of Rayleigh and P-waves show that there is no numerical dispersion for the frequency-wavenumber range mentioned. Further it can be observed that at a value of wavenumber equal to 78.54 (rad/m), the frequency value corresponds approximately 801 Hz (f = 78.54 x 64.08 / 2 π). For a frequency of 801 Hz the value of wavelength λ is exactly equal to 0.08m. Thus it confirms the results shown in the dispersion curves where the frequency is marked at 801 Hz, shows the reflections from the interaction of the uniform to non-uniform grid boundary. The trends mentioned above for time traces, frequency spectra, and f-k plots are observed for all numerical models studied.

Table 2 provides a general idea about the behaviour of Rayleigh wave interaction with void and its effect on dispersion curves when the receiver points are analyzed in sections. An important observation that can be made from the Table is that, the λ values increases as the embedment depth of the void increases and frequency decrease, i.e., considering the case of section 1, width b = 8cm and embedment depth h = 8, 16, and 32cm. For this case the frequency values are f = 114.3, 96.99, and 69.66 while the calculated λ values are λ = 0.56, 0.66, and 0.92. This trend is shown by all the models under consideration, which confirms the idea that as the wavelength increases, frequency decreases for a constant velocity. Comparison of λ_{norm} within sections show that almost all sections follow 1/3rd rule, i.e., the velocity with which each frequency propagates represents the properties of the material that lies about one third of the wavelength. However, this trend is not shown by values in section 2 and 3 for b = 0.08m. Further it can be seen that for a constant embedment depth, the λ_{norm} value for different widths increases as the width increases. This trend is shown by all models under study. Within a section the λ_{norm} values decreases as the embedment depth increases. These trends as a function of void width and embedment depth can be observed in Figure 7. In the Figure, for Section 1 (b = 0.16m and h = 0.08m) and Section 2 (b = 0.16m and h = 0.16m), it can be seen that these two values do not follow the trend as expected. This is due to the fact that the surface displacement values for width b = 0.16m are horizontal displacement values instead of vertical displacement as stated in previous section.

In Table 3, the first important observation is the positive and negative %age change difference values. Except for section 3 having b = 32cm all the sections have positive values. The reason for negative %age difference is based on the identified pattern velocity which has a positive peak with respect to R-wave velocity line as compared to other sections having negative peak with respect to R-wave velocity line. The general trend is that the values decrease as the embedment depth increases. The maximum change is in section 3 for b = 32cm and h = 8, 16, and 32cm. It can be further observed from the Table, as the width of void increases the % change also increases such as for S1b08h08, S1b16h08, and S1b32h08 the value changes from 2.48% to 3.62% and 5.57%. This trend is shown by all models under study. Figure 8, shows the variation of percent change with normalized wavelength (H/λ) as a function of void width and embedment depth. It could be observe that as the width of void increases, percent change in dispersion curve increases and normalized wavelength (H/λ) decreases.

SUMMARY AND CONCLUSION

This study presents results of numerical simulation to identify underground cavities using the MASW test. The numerical simulations were performed on rectangular voids with variable width and depth. The results from the numerical simulations were recorded as surface responses at 101 recording points. These surface responses were numerically processed in a computer package and dispersion curves and frequency wave-number plots were obtained. From these results, pattern identification was done to study the effect of void width and depth at different locations of array.

It can be concluded that the normalized wavelength values decreases as the embedment depth of void

increases. The maximum percent change in ratio of pattern identified velocity to Rayleigh wave for shallow depth can be seen when the width of the void is large as compared to depth of void. This maximum percent changes seen in all three sections i.e., section 1, 2, and 3. Results presented in this paper are preliminary and further investigation is being carried out on models having dimension in three axes. This study would enable to better understand the behaviour of underground voids using the MASW test.

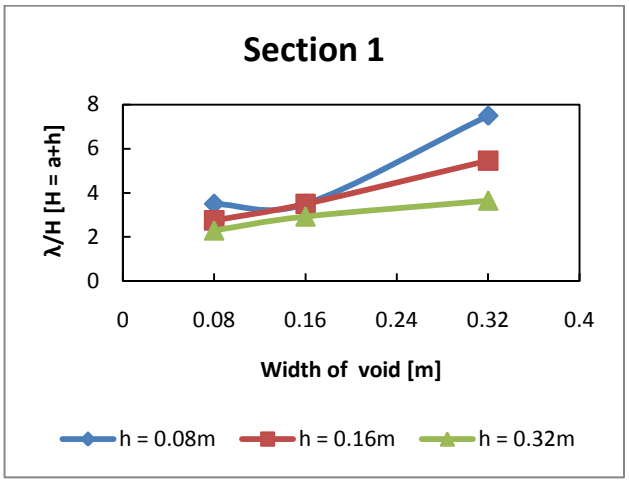

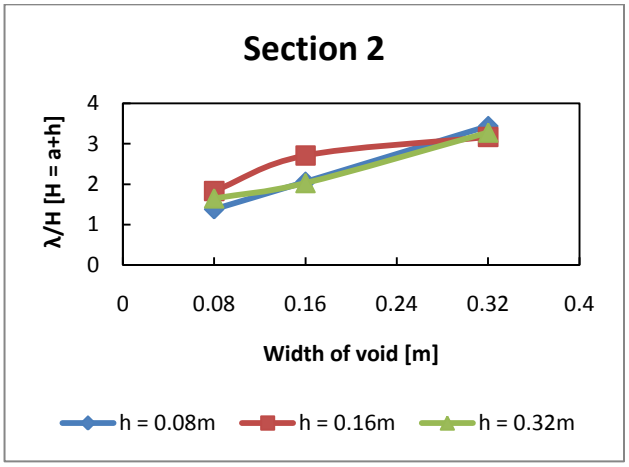

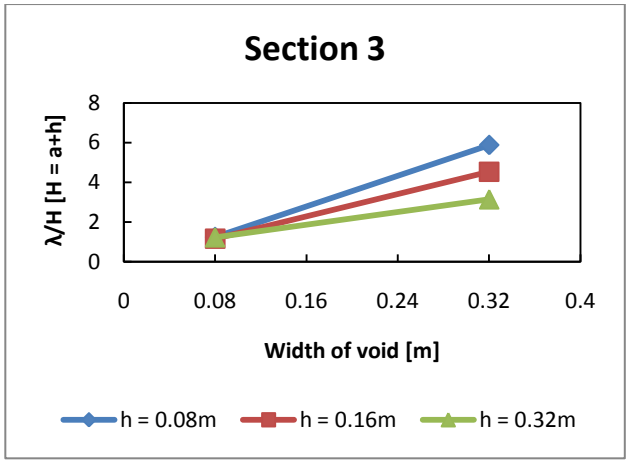

Figure 7: Section 1, 2, and 3 showing variation of width of void to normalized wavelength as a function of embedment depth

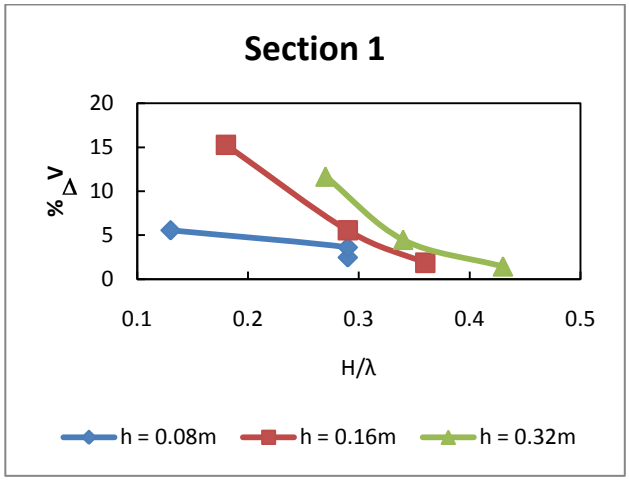

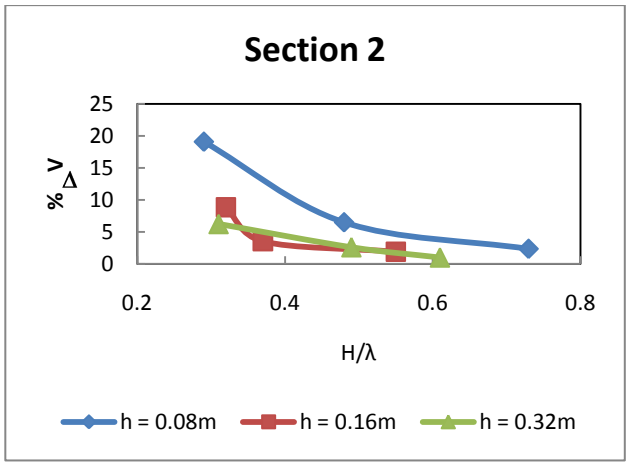

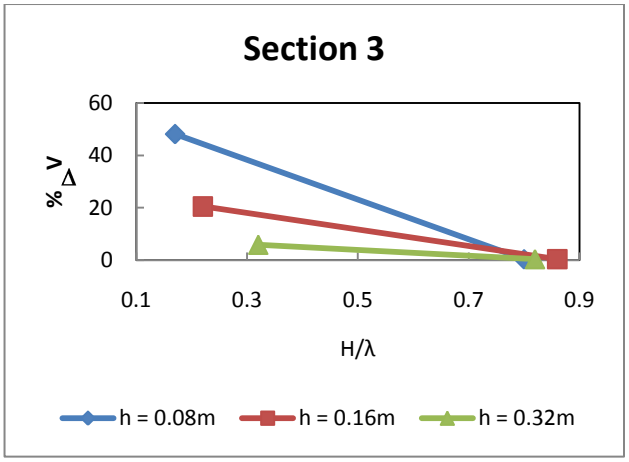

Figure 8: Section 1, 2, and 3 showing variation of percent change to normalized wavelength as a function of width and embedment depth

ACKNOWLEDGEMENT

This research is part of a study on non-destructive testing of geomaterials. Support is provided by the Natural Sciences and Engineering Research Council of Canada (NSERC). Part of this research project was carried out under the Bedrock to Blue Sky – Ultrahigh resolution urban modeling research project at Queen's University, led by Professor Harrap, Department of Geological Sciences and Geological Engineering.

REFERENCES

Cascante, G., Najjaran, H. and Crespi, P. 2006. Nondestructive Evaluation of Brick Walls – Fuzzy Logic Analysis. *Journal of Infrastructure Systems*, ASCE.

Gusunski, N., Ganji, V., & Maher M.H., 1996, Effects of obstacles on Rayleigh wave dispersion obtained from the SASW test. *Soil Dynamics and Earthquake Engineering,* 15(4), 223-231

Hiltunen, D. R., and Woods, R. D. 1989. Influence of source and receiver geometry on testing of pavements by the surface waves method. In A. J. Bush III, and Baladi, G. Y. (Eds.), *Nondestructive testing and backcalculation of moduli*, ASTM STP 1026 (pp. 138-154). Philadelphia: American society of testing and materials.

Itasca, 2000. *Flac: fast Lagrangian analysis of continua users guide. Minneapolis*, Minnesota: Itasca consulting group Inc.

Jones, R. 1962. Surface wave technique for measuring the elastic properties and thickness of roads: theoretical developments. *British Journal of Applied Physics*, 13, 21-29.

Kong, F.N., Westerdahl, H., and By, T.L. 1994. Borehole radar tunnel detection at Gjovik, Norway. *Norwegian Geotechnical Institute, Publication 194*, 1-10.

Lamb, H. 1904. On the propagation of tremors over the surface of an elastic solid. *Philos. Trans. r. Soc. London*, Ser. A, 203, 1-42.

Nasseri-Moghaddam, A., Cascante, G., Phillips, C., Hutchinson, D.J. 2007. Effect of underground cavities on Rayleigh waves – Field and numerical experiments. *Journal of Soil Dynamics and Earthquake Engineering*, Issue 27: 300 - 313.

Nasseri-Moghaddam, A., (2006). Study of the effect of lateral inhomogeneities on the propagation of Rayleigh waves in an elastic medium. (Doctoral dissertation). Retrieved from UWSpace (http://hdl.handle.net/10012/781).

Nazarian, S., Stokoe, K. H. 1984. In-situ shear wave velocities from spectral analysis of surface waves, *Proc. of the Eighth World Conf. on Earthquake Engineering*, San Francisco, California, III, July 21 - 28, pp. 31 – 38.

Park, C. B., Miller, R. D., and Xia J. 1999. Multichannel analysis of surface waves. *Geophysics*, 64(3), 800-808.

Phillips, C., Cascante, G., and Hutchinson, J., 2001, Numerical simulation of seismic surface waves: In 54th Canadian Geotechnical Conference, Calgary, Alberta, September, 1538–1545.

Phillips, C., Cascante, G., and Hutchinson, J., 2004, Evaluation of lateral homogeneity with the distance analysis of surface waves: Canadian Geotechnical Journal, 41(2), 212-226.

Stokoe II, K.H., Nazarian, S., Rix, G.J., Sanchez-Salinero, I., Sheu, J.C., and Mok, Y.J. 1988. In-Situ Seismic Testing of Hard-To-Sample Soils by Surface Wave Method. Earthquake Engineering and soil dynamic II - Recent advances in ground-motion evaluation, Von Thun, J.L (ed), Utah, Geotechnical special publication 20: 264-279.

Santamarina, J., Klein, K., and Fam, M. 2001. *Soils and waves*. West Sussex, Eng: John Wiley and Sons Ltd.

Sheu, J.C., Stokoe II, K.H., and Roësset, J.M., 1988, Effect of reflected waves in SASW testing of pavements: Research Record No. 1196, Transportation Research Board, National Research Council, Washington, D.C., 51–61.

Shokouhi, P., Gucunski, N., 2003, Application of wavelet transform in detection of shallow cavities by surface waves: In Proc. Symposium on the Application of Geophysics to Engineering and Environmental Problems, San Antonio, Texas.

SWAN, 2010: Surface wave analysis: Geostudi Astier S.r.l. Livorno, Italy

Turney, J. E., 1985, Subsidence above inactive coal mines: information for the homeowner: Retrieved Nov. 26, 2004, from http://www.mines.edu/fs_home/tboyd/coal/homeowner.

Table 2. Effect of void size on dispersion curve and normalized wavelength

SEC 1 [h = 0.08m, 0.16m, and 0.32m]														
b = 0.08 m					b = 0.16 m					b = 0.32 m				
Comp	Freq	Vel	$\lambda = V_R/f$	λ/H H = a+h	Comp	Freq	Vel	$\lambda = V_R/f$	λ/H H = a+h	Comp	Freq	Vel	$\lambda = V_R/f$	λ/H H = a+h
S1b08h08	114.3	62.49	0.56	3.50	S1b16h08	114.3	61.76	0.56	3.5	S1b32h08	53.38	60.51	1.2	7.50
S1b08h16	96.99	62.88	0.66	2.75	S1b16h16	76.17	60.52	0.84	3.5	S1b32h16	48.83	54.29	1.31	5.46
S1b08h32	69.66	63.14	0.92	2.30	S1b16h32	54.69	61.2	1.17	2.93	S1b32h32	43.95	56.6	1.46	3.65
No-void	47.61	63.82	1.35		No-void	47	63.82	1.36		No-void	125.7	64.21	0.51	
SEC 2 [h = 0.08m, 0.16m, and 0.32m]														
b = 0.08 m					b = 0.16 m					b = 0.32 m				
S2b08h08	288.1	62.59	0.22	1.38	S2b16h08	195.3	59.93	0.33	2.06	S2b32h08	116.2	51.85	0.55	3.44
S2b08h16	145.2	62.86	0.44	1.83	S2b16h16	98.65	61.82	0.65	2.71	S2b32h16	84.62	58.42	0.76	3.17
S2b08h32	97.66	63.43	0.66	1.65	S2b16h32	79.1	62.4	0.81	2.03	S2b32h32	48.83	60.08	1.31	3.28
No-void	69.34	64.09	0.92		No-void	95.7	64.1	0.67		No-void	122.97	63.97	0.52	
SEC 3 [h = 0.08m, 0.16m, and 0.32m]														
b = 0.08 m					b = 0.16 m					b = 0.32 m				
S3b08h08	327.1	63.87	0.2	1.25	S3b16h08					S3b32h08	68.36	94.92	0.94	5.88
S3b08h16	226.6	63.86	0.28	1.17	S3b16h16	NA				S3b32h16	58.59	77.21	1.09	4.54
S3b08h32	131.8	63.85	0.49	1.23	S3b16h32					S3b32h32	50.78	67.86	1.26	3.15
No-void	60.5	64.11	1.06		No-void					No-void	24.17	64.17	2.65	
* units of frequency in Hz, velocity in m/s, and λ in m														
* V_R = 64.08 m/s														

Table 3. Percentage difference between the values of V_R and pattern identifed velocity

SEC 1 [h = 0.08m, 0.16m, and 0.32m]								
b = 0.08 m			b = 0.16 m			b = 0.32 m		
Comp	$V_{pattern}$	%ΔV	Comp	$V_{pattern}$	%ΔV	Comp	$V_{pattern}$	%ΔV
S1b08h08	62.49	2.48	S1b16h08	61.76	3.62	S1b32h08	60.51	5.57
S1b08h16	62.88	1.87	S1b16h16	60.52	5.56	S1b32h16	54.29	15.28
S1b08h32	63.14	1.47	S1b16h32	61.2	4.49	S1b32h32	56.6	11.67
No-void	63.82	0.41	No-void	63.82	0.41	No-void	64.86	-1.22
SEC 2 [h = 0.08m, 0.16m, and 0.32m]								
b = 0.08 m			b = 0.16 m			b = 0.32 m		
S2b08h08	62.59	2.33	S2b16h08	59.93	6.48	S2b32h08	51.85	19.09
S2b08h16	62.86	1.90	S2b16h16	61.82	3.53	S2b32h16	58.42	8.83
S2b08h32	63.43	1.01	S2b16h32	62.41	2.61	S2b32h32	60.08	6.24
No-void	64.09	-0.02	No-void	64.1	-0.03	No-void	63.97	0.17
SEC 3 [h = 0.08m, 0.16m, and 0.32m]								
b = 0.08 m			b = 0.16 m			b = 0.32 m		
S3b08h08	63.87	0.33	S3b16h08			S3b32h08	94.92	-48.13
S3b08h16	63.86	0.34	S3b16h16	NA		S3b32h16	77.21	-20.49
S3b08h32	63.85	0.36	S3b16h32			S3b32h32	67.86	-5.90
No-void	64.11	-0.05	No-void			No-void	64.17	-0.14